REGIONAL EVENT IDENTIFICATION RESEARCH IN EASTERN ASIA

Steven R. Taylor, Howard J. Patton, Xiaoning (David) Yang, and Monica Maceira

Los Alamos National Laboratory

Sponsored by National Nuclear Security Administration
Office of Nonproliferation Research and Engineering
Office of Defense Nuclear Nonproliferation

Contract No. W-7405-ENG-36

ABSTRACT

We describe ongoing studies of broad-area, regional-event identification in Eastern Asia. The goal of our work is to provide a framework that allows for accurate identification, operational transparency, and clear reporting to nontechnical decision makers. The underlying methodologies need to have a clear physics basis packaged in a sound statistical framework having proper uncertainty estimates. We are developing regional surface-wave discriminants (e.g., m_b - M_s) through a suite of focused studies. The 20-second m_b-M_s discriminant is one of the most reliable and best understood methods for identifying underground nuclear explosions. To extend the discriminant to lower magnitude thresholds at regional distances it is necessary to perform the M_s measurement at shorter periods. Although shorter period Rayleigh wave measurements have lower detection thresholds than those at 20 seconds, they are more influenced by the effects of earthquake depth causing overlap of earthquake and explosion populations. We present a technique using a probability of detection model (PXD) to estimate the probability that a surface wave detection came from an underground explosion. The key to the method is the development of a simple analytic model used to predict the maximum expected amplitude probability distribution (upper tail) from an underground explosion of a given size recorded at a specified distance. For a given sensor we can define the probability of detection given that the source was an explosion. Using Bayes' Rule we can then determine the probability that the signal detection originated from an explosion. Using a hypothesis test, we can compute the conditional probability (represented as a p value) that the detected signal originated from an explosion. We show results of the signal detection formulation using short period Rayleigh waves from earthquakes and explosions in Eurasia and compare to the traditional m_b-M_s at different periods. For a set of earthquakes and explosions recorded at WMQ measured at 6 – 12 seconds period, false alarm rates are reduced from 28% for m_b-M_s to 18% using the probability of detection model.

For our regional m_b – M_s work, multi-frequency surface wave magnitudes M_s have been measured for earthquakes and explosions in southern Asia using the methodologies of Marshall and Basham (1972) and Russell (2004) using regional and far-regional seismograms. Five frequency bands with center periods of 20, 16, 12, 10, and ~7 sec were chosen, and the final M_s corresponds to the band giving the largest M_s or the largest amplitude. In either case, M_s from both methods show good correlation with independently determined seismic moments for the earthquakes. Due to the narrowband filtering criteria used in the Russell method, no corrections for dispersion are necessary and this offers practical advantages over other methods requiring such corrections. We have developed surface-wave attenuation tomographic maps for central and southeast Asia. These maps can be used in the reformulation of regional M_s calculations with two-dimensional (2-D) path corrections to reduce station-magnitude scatter and network-magnitude bias. Compared with one-dimensional (1-D) distance corrections, the use of 2-D attenuation models for path corrections in M_s calculations reduced the station-magnitude scatter by 16% to 18% on the average.

Another component of these studies involved evaluation and refinement of existing surface-wave slowness tomographic models at shorter periods (6 seconds and above) for central Asia. Rayleigh-wave group-velocity dispersion curves are used to compute high-resolution, 0.5-degree cell size, slowness tomographic maps. Using our high-resolution tomographic maps of western China, we investigate the shear velocity structure beneath the Tarim and Junggar basins. Preliminary results show high upper-mantle shear velocities that are usually interpreted as old, cold, thick lithospheric blocks and differences in shear velocities between eastern and western Tarim. To obtain a 3D model and improve resolution, we divide into 1° x 1° cells the entire region comprising the Tarim basin, the Tien Shan, and the Junggar basin. We develop an inversion technique to invert the dispersion curves for all the 1° x 1° cells simultaneously imposing some geophysical constraints such as the gravity anomalies in the region.

OBJECTIVE

The objective of this work is to provide methodologies and calibration parameters for robust regional-event identification at reduced magnitude thresholds.

RESEARCH ACCOMPLISHED

A Probability of Detection Method for Reducing Short Period $m_b - M_s$ False Alarm Rates

The 20-second teleseismic m_b-M_s discriminant is one of the most reliable and best understood methods for identifying underground nuclear explosions. However, at lower magnitudes and regional distances, detection of 20-second surface waves can be very difficult. Short period (SP) Rayleigh waves (6-12 seconds) generally show lower detection thresholds than 20 second Rayleigh waves used to construct $m_b - M_s$ discriminants. The Rayleigh waves from earthquakes are typically expected to be greater than those from explosions because of the shear energy radiated from the faulting process. However, short period surface waves are more strongly affected by earthquake depth resulting in much scatter in the traditional $m_b - M_s$ discriminant. We have developed a technique using a probability of detection model (PXD) to estimate the probability that a surface wave detection came from an underground explosion (Taylor and Patton, 2005). The key to the method is the development of a simple analytic model to predict the maximum expected amplitude probability distribution (upper tail) from an underground explosion of a given size recorded at a specified distance.

The detection classifier can be applied when there is a signal detection, $A_o > N_o$ and the observed amplitude is greater than the maximum expected amplitude, $A_o > A_x^\alpha$ (Equation 1). The right portion of Figure 1 shows an enlargement of the magenta box in the left portion of Figure 1 and illustrates the conditions under which the detection classifier is applicable. It is important to note that the maximum expected amplitude from the explosion can also be greater than the noise as illustrated by the red dashed line. Thus, the PXD method can be applied under the detection conditions

$$D \in \left\{A_o > \max\left(N_o, A_x^\alpha\right)\right\}. \tag{1}$$

Next, for each sensor we define the probability of detection given that the source was an explosion

$$P(D \mid X) = 1 - \int_{-\infty}^{\max\left(N_o, A_x^\alpha\right)} f_x(A)\,dA = 1 - F_x\left(\max\left(N_o, A_x^\alpha\right)\right). \tag{2}$$

Using Baye's Rule we can determine the probability that the signal detection was from an explosion

$$P(X \mid D) = \frac{P(D \mid X)P(X)}{P(D)}. \tag{3}$$

where $P(X)$ is the prior probability that an explosion occurred and $P(D)$ is derived from a probability of detection curve for the signal of interest. For this study we set $P(X)$ and $P(D)$ to be equal.

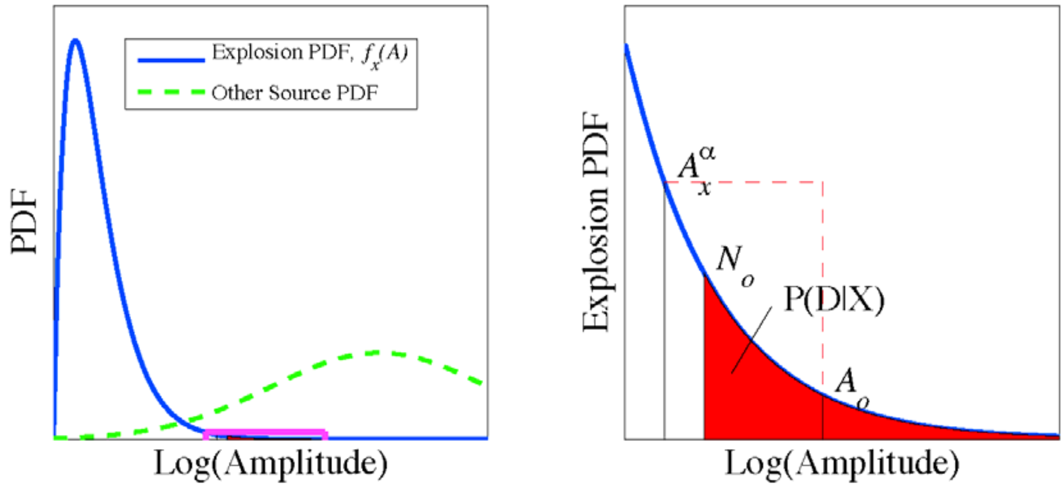

Figure 1. Left: Schematic illustration of expected Probability Density Functions (PDFs) for explosions and another benign source type (e.g. earthquakes). Right: Blowup of magenta box in left figure showing high amplitude tail of explosion PDF and measurements discussed in text. Note that the maximum expected amplitude can also be greater than the noise for the PXD method to be applicable under the detection conditions of Equation 1; $D \in \left\{A_o > \max\left(N_o, A_0^{\alpha}\right)\right\}$ as indicated by the dashed red line.

The next step in the procedure is to develop a simple analytic model to predict the maximum expected amplitude from an explosion of a specified size and distance. The vertical fundamental mode Rayleigh wave displacement spectrum for a step function explosion at depth zero is (Aki and Richards 1980; eq. 7.151)

$$\left|u_z^R(r,\omega)\right| = -\frac{r_2}{8\omega c U I_1}\sqrt{\frac{2}{\pi k r}}\left\{k r_1 + \frac{dr_2}{dz}\right\}M_0^x \tag{4}$$

where $I_1 = \frac{1}{2}\int_0^{\infty} \rho\left(r_1^2 + r_2^2\right)dz$ is the energy integral and r_1 and r_2 are the radial and vertical displacement eigenfunctions, respectively, r is the range, ω is the angular frequency, c is the phase velocity, U is the group velocity, k is the wavenumber and M_0^x is the explosion moment. For a Poisson solid ($\mu = \lambda$) half space, $c = U = 0.92\beta = 0.5308\alpha$ and it can be shown that $r_1 = 0.4227$, $r_2 = -0.6204$, $dr_2/dz = -0.1410k$ and $I_1 = 0.6205(\rho/k)$. Thus, Equation 8 simplifies to

$$\left|u_z^R(r,\omega)\right| = \frac{0.6461 M_0^x}{\rho\alpha^{7/2}\sqrt{Tr}} \tag{5}$$

where T is the period. Using the shorthand $\left|u_z^R(r,\omega)\right| = A_s(T)$ and taking the base 10 logarithm of Equation 5 gives

$$\log A_s(T) = \log M_0^x - \frac{1}{2}\log Tr - \log \rho\alpha^{7/2} - 0.1897 \tag{6}$$

Next, we will add three new terms to Equation 6, the first representing the maximum expected contribution to the Rayleigh wave amplitude for tectonic release (or other secondary sources), a second term converting spectral amplitude to peak-to-peak (P-P) amplitude and an attenuation operator.

Thus after adding the tectonic release term and the conversion from spectral amplitude to P-P and an attenuation operator Equation 6 becomes

$$\log A_{pp}(T) = \log M_0^x - \frac{1}{2}\log Tr - \frac{\pi \log e}{Q(T)U(T)T} r - \log \rho\alpha^{7/2} + \log A_T - \frac{1}{2}\log\frac{T_w}{B} + \log A_{pp/rms} - 0.1897 \tag{7}$$

where $\log A_{pp/rms}$ is the conversion from RMS to P-P amplitude. From the attenuation term in Equation 7 it is evident that attenuation and group velocity tomography can be used in the estimation of the maximum expected amplitudes.

To illustrate the PXD method, we selected a data set of 6 to 12 second period Rayleigh wave P-P amplitude measurements from station WMQ in western China. The dataset and measurements are described in Hartse et al., (1997). The P-P measurements were converted to M_s using Rezapour and Pearce (1998). We next assess the performance of the short-period single station $m_b - M_s$ discriminant at WMQ by basically following a similar but simplified methodology of that outlined by Fisk et al., (2002). To do this we assign a critical value of $m_b - M_s$ to be that of the lowest explosion below which all events are declared earthquake. A histogram of the $m_b - M_s$ values at WMQ is shown in Figure 2. The critical value in this case is set to be $m_b - M_s = 0.61$ resulting an estimated false alarm rate, $P(X|Q) = 0.283$ (or 28.3%). Note that this value of $P(X|Q)$ is higher than the approximate value of 20% in Fisk et al., (2002). Of course, none of the explosions are misclassified, $P(Q|X) = 0$. Interestingly, using PXD by itself as an earthquake identifier, 78% of all events are assigned a p value resulting in a false alarm rate of 22% that is better than $m_b - M_s$ alone for this dataset.

Figure 3 shows the results of the PXD analysis portrayed on an $m_b - M_s$ plot versus m_b and distance (using snr cutoff of 2). We have taken some liberties with our probabilistic notion, but in the figure $P(X|Q)$ indicates calling an event an explosion when it is actually an earthquake (false alarm), $P(Q|X)$ indicates calling an event an earthquake when it is in fact an explosion (missed explosion), and $P(Q|Q)$ and $P(X|X)$ are correctly classified earthquake and explosions, repectively. $P(X|X)$ actually means that an explosion was not assigned a p value. For the PXD method the $P(X|Q)$ is reduced from 28.3% down to 18.6%.

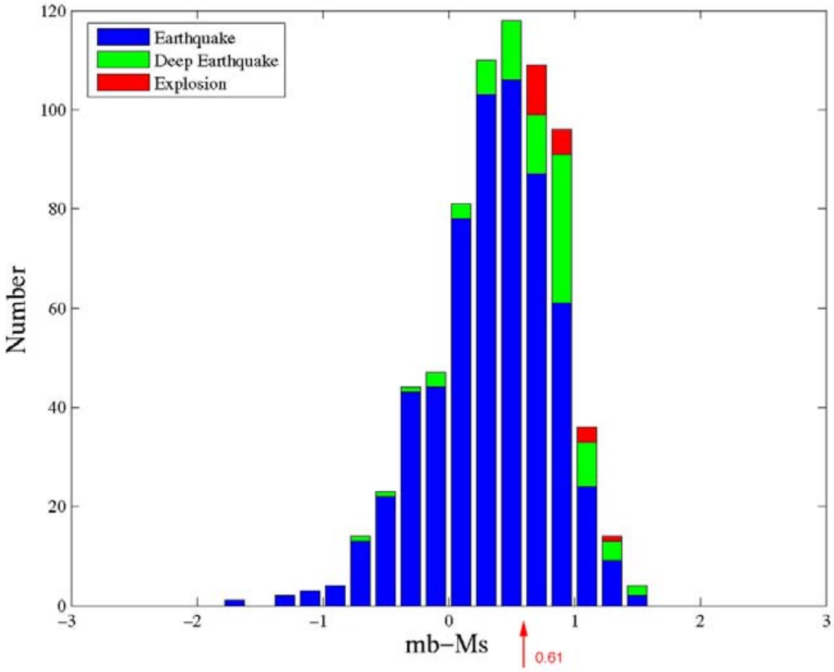

Figure 2. Histogram for $m_b - M_s$ data. Critical point for $m_b - M_s$ discriminant test set to 0.61 (the lowest explosion value).

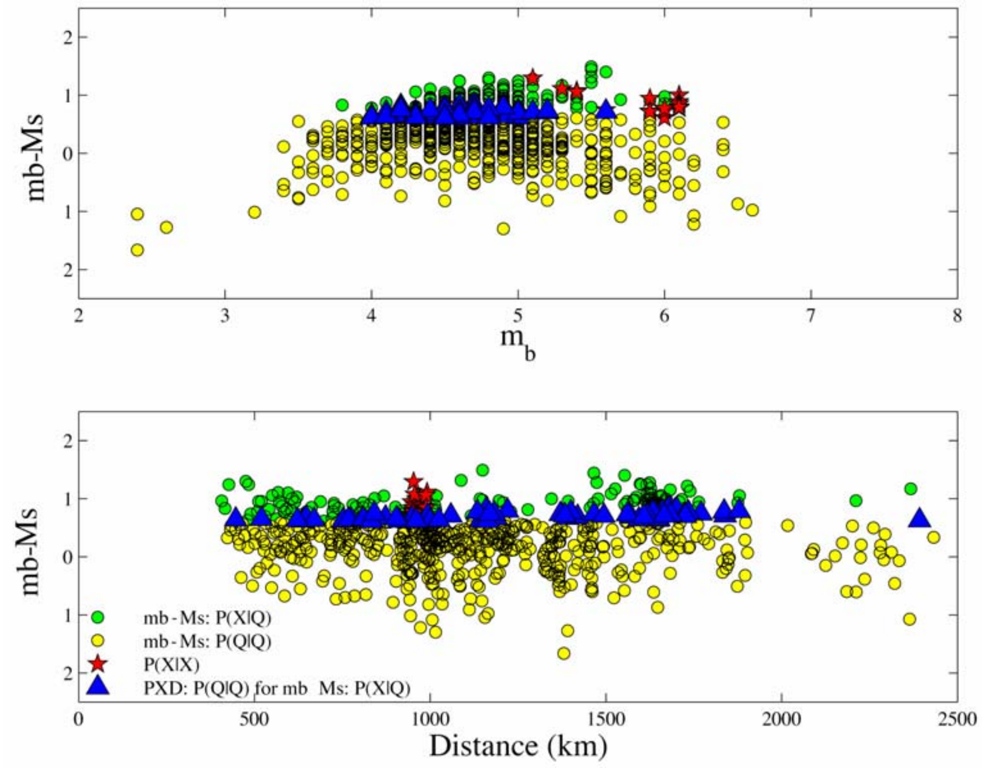

Figure 3. Comparison of $m_b - M_s$ and PXD results (see text for details).

Regional $m_b - M_s$

The M_s work reported on in this paper is part of LANL's development and evaluation of regional $m_b - M_s$ data sets for key stations and monitoring areas in Asia to ascertain their discrimination capabilities at small magnitudes. Traditionally M_s is measured in the 20 s passband, but regional-distance applications offer the promise to lower the magnitude threshold that M_s can be measured through the implementation of multi-frequency M_s methodologies coupled with better corrections for propagation effects of intermediate-period (20-7 s) surface waves. New M_s methodologies (e.g., Russell, 2004) and tomographic inversions of surface wave group velocities and attenuation coefficients in Asia (e.g., Levshin and Ritzwoller, 2003; Yang et al., 2004) have advanced the state-of-the-art to where regional M_s calibrations should yield fruitful results for future discrimination studies.

In this application, five passbands were selected for measuring multi-frequency M_s, and these passbands had center periods of 20, 16, 12, 10, and 8 s. M_s was calculated in two ways: (1) the well-known method due to Marshall and Basham (1972), and (2) a new method due to Russell (2004). The Marshall and Basham M_s formula is

$$M_s = \log(A) + B^{'}(\Delta) + P(T) \tag{8}$$

where A is the maximum amplitude in nm measured off the displacement Rayleigh wave train, $B'(\Delta)$ is a distance correction accounting for spreading on a sphere, dispersion, and absorption, and $P(T)$ is an additional dispersion correction, T is wave period in s, U group velocity in km/s, and Δ distance in degrees. The Russell M_s formula is taken from Eq. 57 of the 2004 report

$$M_{s(b)} = \log(a_b) + \frac{1}{2}\log(\sin(\Delta)) + 0.0031\left(\frac{20}{T}\right)^{2.3}\Delta - 0.66\log\left(\frac{20}{T}\right) - \log(f_c) - 0.43 \tag{9}$$

where f_c is the corner frequency of a three-pole, two-pass Butterworth filter used to filter the displacement Rayleigh wave train before measuring the maximum zero-to-peak amplitude, a_b, in nm. The Butterworth filter is designed to minimize the effects of dispersion by choosing an f_c such that $f_c \leq 0.6 / T\sqrt{\Delta}$, where the minimum value of G (see Eq. 44 of the 2004 report) is ~0.6 for most continental paths and wave periods, $8 < T < 25$ s. In the case of Marshall and Basham M_s (M-B M_s), the corner frequencies of the Butterworth filters were held fixed and correspond to the following period ranges: 23-17, 19-13, 14-10, 12-8, and 9-5. The corner frequencies f_c for the Russell M_s (DR M_s) are dynamic in the sense that they depend on path length, as well as center period.

We processed 365 seismic waveforms recorded at four stations (BRVK, MAKZ, MK31, and WMQ) from 111 earthquakes and 56 explosions distributed in southern Asia for the most part. Both long-period (1 s/s) and broadband (40 s/s) channels were used. Waveforms from the Borovoye Archive (Kim et al., 2001) are for the DS seismometer system with 20-s natural period and ~3-s sampling rate. Forty-nine of the 111 earthquakes have seismic moment M_o estimates from regional studies of Ammon et al. (2003). The remaining earthquakes are those with usable surface waves from the ENSCO dataset. The vast majority of explosions are from the Semipalatinsk test site. Three-component waveforms were corrected for instrument response and rotated to the great-circle path. The following describes the processing steps taken to measure amplitude and period used in the M_s formulas. The processing begins by filtering the displacement waveforms into five passbands, and proceeds to operate independently on each of the filtered waveforms. For particle motion processing, the product of the Hilbert-transformed radial component with the vertical component is taken, and the absolute value of the resulting time series is passed through a band-reject filter to obtain a smooth envelope function where the largest amplitudes correspond to times consistent with Rayleigh particle motion. This envelope function is converted to a unit boxcar trace using an amplitude threshold set to 1/2 the maximum value of the envelope time series. For group velocity processing we chose to apply group velocity windowing, where time windows were computed using slowness predictions from tomographic models developed for Eurasia (Ritzwoller and Levshin, 1998; Stevens et al., 2001; Levshin and Ritzwoller, 2003) on a path-by-path basis. Minimum and maximum slowness values were found for the frequency band in question, and these values were adjusted to account for uncertainty in the predicted estimates. The measurement window corresponds to a time range consistent with Rayleigh particle motion and the tomographic predictions of Rayleigh group arrivals. An amplitude measurement for M_s is legitimate only on that portion of the waveform lying inside a measurement window. A few simple rules were used to construct the measurement window from the particle motion and group velocity windows discussed above. If there is no intersection between the arrival time window and a particle motion window, the result is a "null" trace and no amplitude measurement is made.

The final M_s were determined from either maximum magnitude or maximum amplitude criteria. In the case of M-B M_s, a magnitude was computed for each of the four utilized passbands, and the band yielding the largest magnitude was selected. The DR M_s is based on the passband with the largest amplitude. No attempt was made to compute network M_s from the limited number of stations calibrated so far. Further testing of our M_s measurements was performed by (1) comparing M-B M_s with DR M_s, (2) comparing M_s with independently determined log M_o, and finally (3) plotting M_s versus m_b. M-B M_s versus DR M_s for all 365 seismic waveforms plot with unit slope showing that the two sets of M_s values scale identically, as we would expect. DR M_s are on average 0.23 magnitude units (mu) larger than M-B M_s. This difference would have been even larger if the final M-B M_s had been computed from maximum amplitude, like DR M_s was, instead of maximum magnitude.

The correlation plots of DR M_s against log M_o are shown in Figure 4. One plot is for DR M_s based on maximum amplitude and the other is for DR M_s based on maximum magnitude. Assuming a slope of 1.0, the root-mean-squared residual scatter about the line is 0.25 mu and 0.27 mu, respectively. Thus there is not a reason to favor maximum amplitude over maximum magnitude based on these results. For reference, M-B M_s has an RMS scatter of 0.27 mu, very similar to DR M_s. A plot of DR M_s versus m_b for earthquakes and explosions in Figure 5. As expected, for a given M_s explosions have larger m_b than earthquakes do. For these single-station M_s measurements, the earthquake population shows much more scatter than the explosion population. This is due to variations in source radiation patterns and path effects since the earthquakes are located over a much wider area than the explosions, the majority being detonated at the Semipalatinsk test site. Another source of scatter for the earthquakes is focal depth, with deep earthquakes less efficient exciting surface waves than shallow ones. While the scatter is great and many earthquakes may not have reliable depth determinations, there appears to be some tendency for deeper earthquakes to have smaller M_s for their m_b.

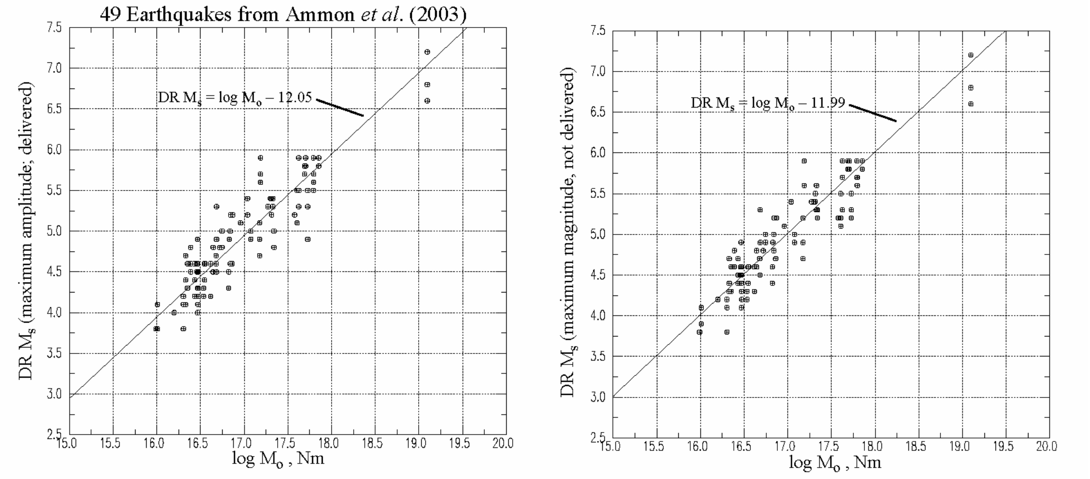

Figure 4. Plots of DR M_s versus log M_o. The left plot is for DR M_s based on maximum amplitude, while the right plot is DR M_s based on maximim magnitude.

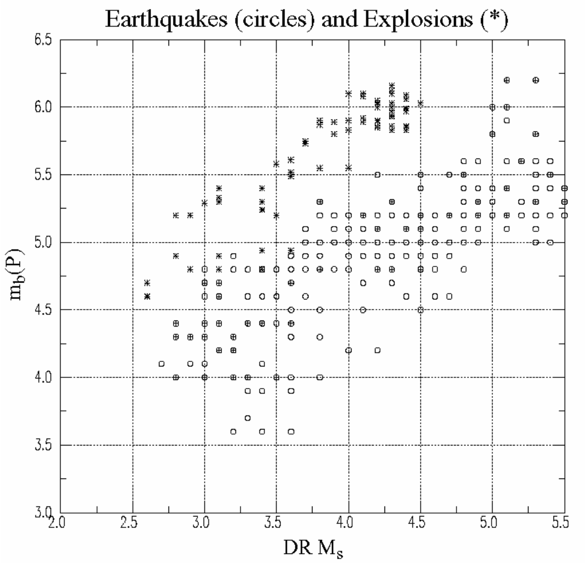

Figure 5. M_s -m_b plot for selected earthquakes and explosions in Asia. Deep earthquakes (> 50 km) are plotted as circles with a cross enclosed. m_b are catalog values for earthquakes and non-Semipalatinsk explosions. Atomic Weapons Establishment m_b are used for Semipalatinsk explosions.

Application of Rayleigh-Wave Slowness Tomography to the Determination of the Shear-Velocity Structure of Central Asian Basins

We investigate the shear velocity structure of the crust and upper mantle beneath two main central Asia sedimentary basins from surface wave velocity inversions. We have developed short-period (6 to 30 s) high-resolution, half-degree cell size, slowness tomographic maps of fundamental mode Rayleigh waves for a region in northwestern China (Maceira et al., 2005). We extended the computation of the tomographic maps to longer periods up to 100 s. Our computed Rayleigh wave slowness tomography models show unprecedented resolution that reveals greater geologic detail than has previously been achieved using surface waves, and which give us insight into the shear-velocity structure of the crust underlying this part of Asia.

We used these slowness models to predict group velocity dispersion curves along 13 specific paths through the Tarim basin, western China. Using an iterative, stochastic, least square inversion technique (Herrmann, 1988), we inverted the group velocity dispersion curves for the 1D shear velocity structure profiles. Figure 6 shows the velocity profile resulting from one of the inversions. The fit to the data is very good. Placing all the resulting profiles together, we can get a 2D image of the shear velocity versus depth, which clearly shows differences between the east and west Tarim basin (Figure 7). The same type of study for the Junggar basin, northwest China, shows a simpler image with high upper-mantle shear velocities that are usually interpreted as old, cold, thick lithospheric blocks.

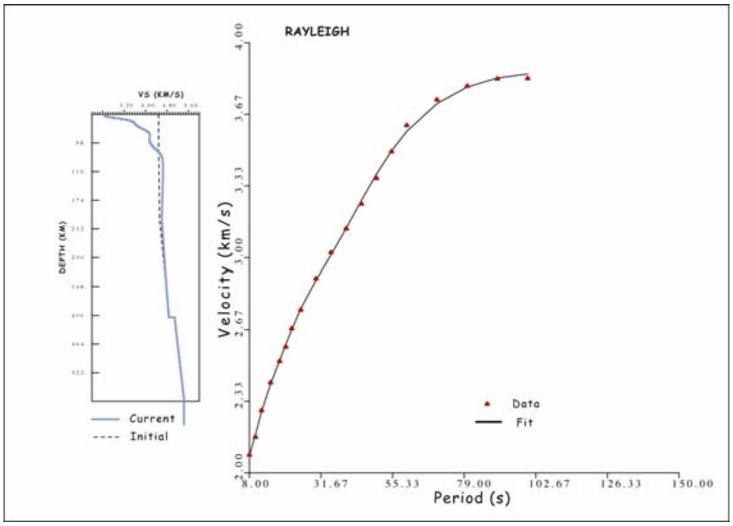

Figure 6. Schematic diagram showing 1D shear-velocity profile for a specific path along the Tarim basin (left) and the fit to the Rayleigh wave dispersion measurements used for the specific inversion (right).

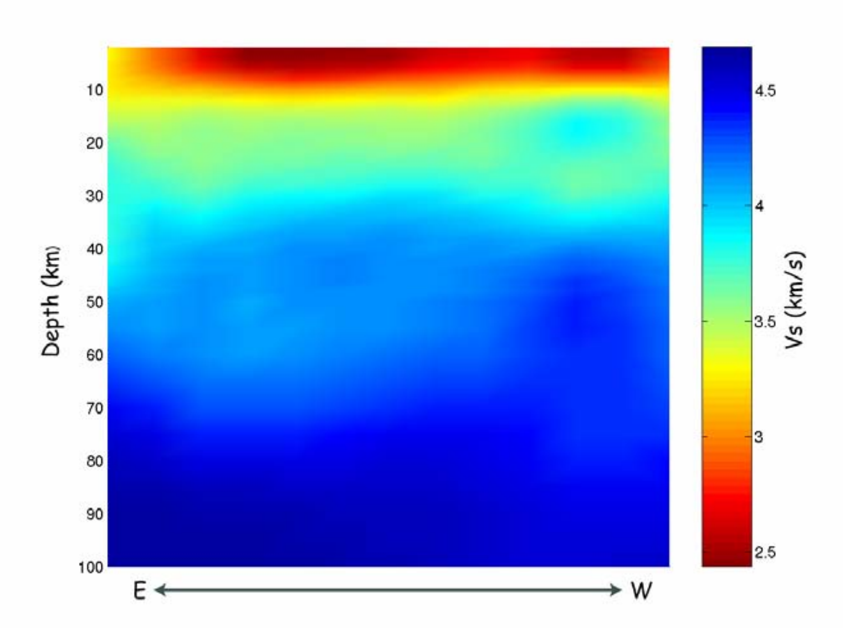

Figure 7 2D image of the shear velocity versus depth along an east-west direction through the Tarim basin. Differences between east and west Tarim are evident not only on the surface but also deeper into the lower crust and upper mantle.

To obtain a 3D model and improve resolution, we now divide into 1º x 1º cells the entire region comprising the Tarim basin, the Tien Shan, and the Junggar basin. Figure 8 shows different images of the 3D model when we invert the dispersion curves for all the cells simultaneously. We are right now working on the developing of a new inversion technique, which will allow us to jointly invert surface wave dispersion measurements and gravity anomalies observations in the region. Improved knowledge of the shear velocity structure of these two sedimentary basins is of fundamental importance for understanding and posing constraints on possible models of geodynamic evolution. Furthermore, the improved 3D shear velocity model will help in the better location determination of epicenters applicable to different seismological studies.

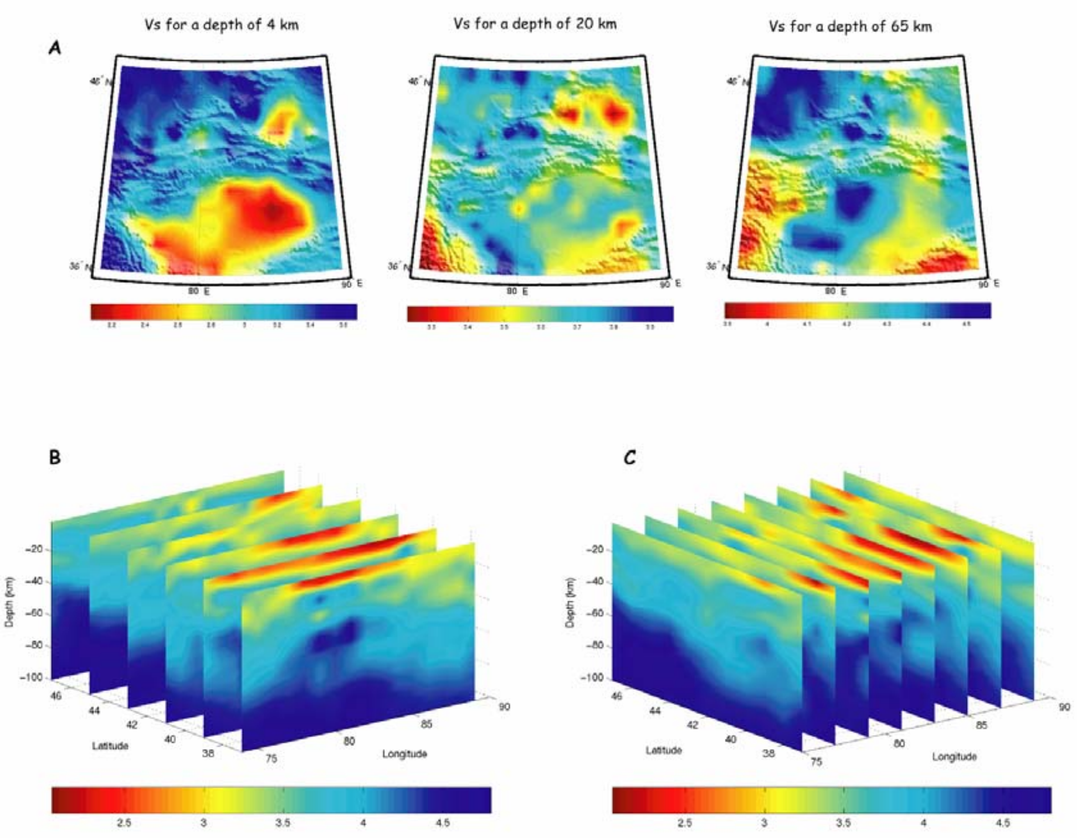

Figure 8 3D shear velocity model for the region in northwestern China comprising the Tarim basin, the Tien Shan, and the Junggar basin. A) shear velocity model slices at 4, 20, and 65 km depth; B) shear velocity model plotted at different latitudes; C) shear velocity model plotted at different longitudes. Note that the color scale is different for each image.

CONCLUSIONS AND RECOMMENDATIONS

Event identification studies in Eastern Asia involve development of algorithms for constructing discriminants as well as applying the algorithms for station calibration. Our research outlined in this paper has focused on regional seismic discrimination using regional $m_b - M_s$ discriminants and MDAC corrected amplitudes. Our ongoing work in the development of regional $m_b - M_s$ discriminants will build upon the surface-wave attenuation model and short-period surface-save slowness maps that we have developed.

REFERENCES

Aki, K. and P. G. Richards. *Quantitative Seismology. Theory and Methods,* W.H. Freeman and Co., New York, NY, 1980.

Ammon, C., G. Randall, and J. Julia (2003). Improving estimates of depth, magnitude, and faulting parameters of earthquakes in central Asia, in *Proceedings of the 25th Seismic Research Review—Nuclear Explosion Monitoring: Building the Knowledge Base*, LA-UR-03-6029, Vol. 1, pp. 24-33.

Fisk, M.D., D. Jepsen, and J.R. Murphy, Experimental seismic event-screening criteria at the Prototype International Data Center (2002), *Pure. App. Geophys*., 159, 865-888.

Hartse, H.E., S.R. Taylor, W.S. Phillips, and G.E. Randall (1997), Regional event discrimination in central Asia with emphasis on western China, *Bull. Seism. Soc. Am.*, 87, 551-568.

Herrmann R. B. (1988), Surface wave inversion program, *Computer Programs in Seismology*, Vol. IV, Saint Louis University, Saint Louis, Missouri.

Kim, W.-Y., P. G. Richards, V. Adushkin, and V. Ovtchinnikov (2001). Borovoye digital archive for underground nuclear tests during 1966-1996, Data report on the web at http://www.ldeo.columbia.edu/res/pi/Monitoring/Data/brv_exp_archive.html, Borovoye Archive for UNT (information product in PDF).

Levshin, A. L. and M. H. Ritzwoller (2003). Discrimination, detection, depth, location, and wave propagation studies using intermediate period surface waves in the Middle East, Central Asia, and the Far East, Technical Report DTRA-TR-01-28, 120 pp., Defense Threat Reduction Agency, Fort Belvoir, Virginia.

Maceira, M., S.R. Taylor, C.J. Ammon, X. Yang, and A.A. Velasco (2005), High resolution surface wave slowness tomography in central Asia, *J. Geophys. Res*., 110, B06304, doi:10.1029.

Marshall, P. D. and P. W. Basham (1972). Discrimination between earthquakes and underground explosions employing an improved Ms scale, *Geophys. J. R. Astr. Soc.* 28: 431-458.

Rezapour, M. and R. G. Pearce (1998), Bias in surface-wave magnitude M_s due to inadequate distance corrections, *Bull. Seismol. Soc. Am.* 88: 43-61.

Ritzwoller, M. H. and A. L. Levshin (1998), Eurasian Surface Wave Tomography: Group Velocities, *J. Geophys. Res.* 103: 4839-4878.

Russell, D. R. (2004). Theoretical analysis of narrow-band surface wave magnitudes, AFTAC-TR-04-004, Air Force Technical Applications Center, Patrick Air Force Base, FL.

Stevens, J. L., D. A. Adams, and G. E. Baker (2001), Improved surface wave detection and measurement using phase-matched filtering with a global one-degree dispersion model, in *Proceedings of the 23rd Seismic Research Review: Worldwide Monitoring of Nuclear Explosions*, LA-UR-01-4454, Vol. 1, pp. 420-430.

Taylor, S.R. and H.J. Patton (2005), A probability of detection method for reducing short period $m_b - M_s$ false alarm rates, Los Alamos National Laboratory, *LA-UR-05-0236*, submitted to *Bull. Seism. Soc. Am.*

Yang, X., S.R. Taylor, and H.J. Patton (2004), 20-sec Rayleigh-wave attenuation tomography for central and southeast Asia, *J. Geophys. Res*. 109: B12.